Remote Sensing of Environment 247 (2020) 111937

Contents lists available at ScienceDirect

Remote Sensing of Environment

journal homepage: www.elsevier.com/locate/rse

Scalable mapping and monitoring of Mediterranean-climate oak landscapes with temporal mixture models

Daniel Sousa[a,b,*], Frank W. Davis[c,d]

[a] National Center for Ecological Analysis and Synthesis, 735 State Street #300, Santa Barbara, CA 93101, United States of America
[b] Earth Research Institute, UC Santa Barbara, Santa Barbara, CA 93101, USA
[c] La Kretz Research Center at Sedgwick Reserve, 3566 Brinkerhoff Ave, Santa Ynez, California 93460, USA
[d] Bren School of Environmental Science and Management, UC Santa Barbara, Santa Barbara, CA 93106, USA

ARTICLE INFO

Keywords:
Mediterranean ecosystems
California
Oak woodland
Savanna
Phenology
Landsat
Sentinel

ABSTRACT

Mediterranean-climate oak woodlands are prized for their biodiversity, aesthetics, and ecosystem services. Conservation and maintenance of these landscapes requires accurate observations of both present and historic conditions capable of spanning millions of hectares. Decameter optical satellite image time series have the observational coverage to meet this need, with almost 40 years of intercalibrated global observations from the Landsat program alone. However, the optimal approach to leverage these observations for oak ecosystem monitoring remains elusive. Temporal mixture models (TMMs) may offer a solution. TMMs use a linear inverse model based on temporal endmembers (tEMs) chosen to optimize both parsimony and information content by 1) possessing clear biophysical meaning, and 2) accurately representing the variance structure of the observations in the temporal feature space (TFS) composed of low-order Principal Components. We apply this approach to oak woodlands of the California Sierra Nevada foothills. Low-order TFS structure across the ≈1200 km^2 study area is consistently bounded by 4 tEM phenologies: annual grasses, evergreen perennials, deciduous perennials + shadow, and unvegetated areas. Satellite-based tEM phenologies correspond to ground-based PhenoCam time series (correlations 0.8 to 0.9). Systematic temporal decimation is conducted to simulate years with varying numbers of cloud free measurements. Fractional cover of temporal endmembers is observed to scale linearly using as few as 6 images per year and coarse feature space topology is retained with as few as 4 well-timed images per year. In comparing 10 m versus 30 m pixel resolution, linear scaling is observed with correlations of 0.78–0.95. Comparison of 10 m Sentinel-2 and LiDAR-derived tree cover estimates at San Joaquin Experimental Range shows a correlation of 0.74. Visual orthophoto validation shows accuracies of annual, deciduous, and evergreen cover fractions of 74–88% (n = 102). Multi-year analysis of August imagery at Sequoia National Park to investigate dynamics associated with the 2012–2016 drought reveals 5 tEMs corresponding to: steady growth, steady decline, early decline then regrowth, persistent vegetation, and no vegetation. Validation images are sparse, but where available show accuracies in the 88 to 91% range for decrease, growth, and persistently vegetated multiyear endmembers (n = 102). Decreases are observed in areas with oak mortality documented in a recent field-based study. Overall, our results suggest the TMM approach has promise as an accurate, explainable, and linearly scalable method for retrospective analysis and prospective monitoring of Mediterranean-climate oak landscapes.

1. Introduction

Mediterranean-climate oak woodlands and savannas are the focus of considerable scientific, social, and aesthetic interest. Covering approximately 4 million hectares in California and 3 million hectares in Spain and Portugal (Marañón et al., 2009), oak systems host thousands of understory plant and animal species (California Department of Fish and Wildlife (CDFW), 2014; Guisti et al., 1996; Swiecki et al., 1997). As a consequence of their broad spatial extent and exceptional biodiversity, oak woodlands and savannas are a key component of the designation of both the California Floristic Province and Mediterranean Basin as global biodiversity hotspots (Baldwin, 2014; Myers et al., 2000). In addition to their ecological importance, Mediterranean-climate oak landscapes are important pastoral landscapes and also

* Corresponding author at: National Center for Ecological Analysis and Synthesis, 735 State Street #300, Santa Barbara, CA 93101, United States of America.
E-mail address: sousa@nceas.ucsb.edu (D. Sousa).

https://doi.org/10.1016/j.rse.2020.111937
Received 25 March 2020; Received in revised form 5 May 2020; Accepted 2 June 2020
0034-4257/ © 2020 Elsevier Inc. All rights reserved.

recognized for their intrinsic aesthetic and historic value (Allen-Diaz et al., 2007; Davis et al., 2016; Pavlik et al., 1993).

Maintaining Mediterranean-climate oak landscapes is challenging given the number of potential drivers of change. Some agents, such as drought and fire, have existed for millennia and may be amplifying (Borchert and Davis, 2018; Klausmeyer and Shaw, 2009; Loarie et al., 2008; Mensing, 2006; Miller et al., 2009). Other processes, like suburban sprawl (Cameron et al., 2014; Gaman and Firman, 2006) and introduction of nonnative pests (Swiecki et al., 1997), are more recent threats. The confluence of such factors, including observed low recruitment rates of some oak species (Tyler et al., 2006), could significantly alter the extent and composition of oak landscapes. Understanding both past and ongoing effects of these change drivers can both provide valuable context for predicting future impacts and help guide conservation efforts.

Quantitative evaluation of change at a landscape scale requires accurate and spatially extensive methods for both retrospective analysis and prospective monitoring. While optical remote sensing has been used for decades for this purpose, recent advances in data availability and quality have substantially increased the capability of satellite imaging systems. Many of these developments are associated with the Landsat program, including the opening of the Landsat archive (Wulder et al., 2012); rigorous radiometric intercalibration (Chander et al., 2009); subpixel geolocation and terrain correction (Storey et al., 2014); and standardized atmospheric correction routines (Vermote et al., 2018; Vermote and Saleous, 2007). In addition, the 2015 and 2016 launches of Sentinel-2a and -2b (Drusch et al., 2012), along with the European Space Agency's free data availability policy (Berger et al., 2012), provide increased spatial resolution and substantially shortened revisit time. Considerable effort has also been devoted to merging the Landsat and Sentinel-2 data streams, including the development of the Harmonized Landsat Sentinel-2 (HLS) product (Claverie et al., 2018). Taken together, these developments have been heralded as a "paradigm shift" in optical remote sensing (Woodcock et al., 2019), offering new opportunities to improve our understanding of oak landscapes in both California and the Mediterranean region.

Advances in imaging systems and data availability have been accompanied by a concomitant increase in research on remote sensing of oak woodlands and Mediterranean-climate ecosystems. A plethora of monitoring and analysis methods have been proposed for Mediterranean landscapes. Many of these methods are based on change detection from image pairs or relatively small numbers of images (e.g. Berberoglu and Akin, 2009; Recanatesi et al., 2018). While useful for mapping changes associated with specific events, these methods do not fully exploit the dense image time series that are now available. Other methods focus on aerial orthophoto, imaging spectroscopy, and/or LiDAR surveys (e.g. Asner et al., 2016; Bogan et al., 2019; Fricker et al., 2019; Miraglio et al., 2020; Navarro et al., 2019; Swatantran et al., 2011). These studies have achieved impressive results, but remain spatially and temporally limited until data coverage expands considerably – and even then will not allow for retrospective analysis. Finally, highly generalized approaches to automated operational monitoring (e.g. Koltunov et al., 2019; Verbesselt et al., 2010) are under continuous development and can be a useful tool for land managers. However, they are intentionally designed not to be tailored to specific ecosystem types. The need still exists for a method that is tailored to oak woodland and savanna landscapes and can efficiently map and monitor change at regional scales using existing multispectral satellite image time series.

Temporal mixture models (TMMs) may offer a parsimonious solution. TMMs (Piwowar et al., 1998; Quarmby, 1992; Quarmby et al., 1992) represent each pixel time series as a linear combination of constituent endmember temporal processes. Using spatiotemporal characterization (Small, 2012) and knowledge of the landscape, the endmember processes can be chosen to represent straightforward, intuitive landscape components (e.g. distinct vegetation phenologies). Unlike many commonly used complex, multilayered statistical mapping algorithms, the TMM approach rates highly on the metric of "explainability" (Gunning, 2017), a factor deemed increasingly important by data scientists. TMMs are most useful when objects on the landscape are: 1) spatially mixed at the scale of the pixel, and 2) more distinct temporally than spectrally. These conditions are met in many Mediterranean-climate oak landscapes where plant communities may be spatially heterogeneous and spectrally indistinct, but phenologically variable. Previous studies have implemented TMMs for the mapping of impervious surfaces (Li and Wu, 2014; Yang et al., 2012), arctic sea ice (Chi et al., 2016; Piwowar et al., 1998), seasonal cloud forest/grassland systems (Sousa et al., 2019), agricultural dynamics (Jain et al., 2013; Lobell and Asner, 2004; Quarmby et al., 1992; Sousa and Small, 2019), and tropical mangrove forests (Small and Sousa, 2019), with promising results. To our knowledge, however, TMMs remain untested both for Mediterranean systems in general and for California oak landscapes in particular.

In this work, we examine the TMM approach to the mapping and monitoring of Mediterranean-climate oak landscapes. We focus on the California Sierra Nevada foothill oak woodland system (hereafter "Sierra foothills") for reasons outlined below. Specifically, this work addresses the following questions:

1) *Characterization*: What are the dominant spatiotemporal modes of variability in these landscapes, as captured by decameter multispectral satellite image time series? Which, and how many, unique phenological signatures can be reliably identified? How do temporal endmembers derived from satellite image series compare to independent ground-based phenology measurements?
2) *Stability & Scaling*: How does this characterization change across the ~500 km extent of the study area? With decreased temporal sampling frequency? How do mapping results compare between 10 m (current & future Sentinel-2) and 30 m (historic & current Landsat) spatial scales?
3) *Validation and Comparison*: How does single-year mapping accuracy compare against canopy height models derived from small-footprint airborne LiDAR? How do estimates of drought-associated defoliation compare to airphotos and meter resolution satellite images?

2. Background

2.1. Study area

The same landscape complexity that imparts much of the value of oak landscapes also substantially complicates monitoring efforts. Oak landscapes span a wide range of climate zones, elevations, soil types, and land ownership regimes. Individual oaks span a broad continuum of morphologies and sizes: for instance, oak canopies can range from shrublike, < 1 m diameter to arborescent, > 30 m diameter. Tree heights can also vary at a similar scale. Structurally, oak landscapes range from open, grass-dominated savannas with sparse tree cover to dense, closed canopy woodlands and forests. Trees can occur in monospecific or mixed stands. Oak species can be evergreen, seasonally deciduous, and/or drought-deciduous. Substantial phenologic variation exists within species and even within canopies of individuals. Any comprehensive analysis and monitoring approach must contend with this formidable multiscale complexity.

One approach to accommodate this diversity is to decompose the full spatial domain of oak woodlands and savannas into smaller subregions with more manageable properties. California's Sierra Nevada foothills (white outline in Fig. 1) is one such subregion. This area is largely under private ownership and predominantly managed for cattle ranching, but in recent decades the Sierra foothills have also experienced extensive conversion from oak woodlands to rural residential development, especially areas east of Sacramento (Cameron et al., 2014; Gaman and Firman, 2006). Extreme drought from 2013 to 2016

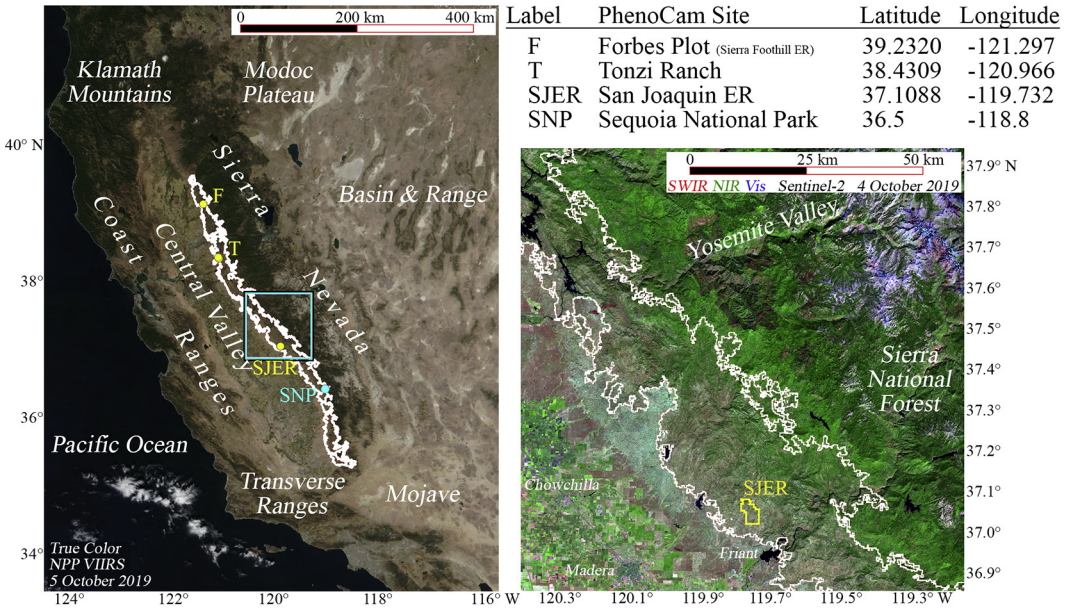

Fig. 1. Index map. White outline shows approximate extent of Blue Oak (*Quercus douglasii*) in woodlands, savannas, and grasslands of the Sierra Nevada foothills. Yellow dots indicate PhenoCam locations used in Figs. 3 and 4. Black/cyan box and right panel show extent of the Sentinel-2 tile (11SKB) containing the San Joaquin Experimental Range (SJER, yellow dot and vector), used for the single-year mapping example in Figs. 5, 7a, 8 and 9. Cyan dot shows approximate location of Sequoia National Park (SNP), site of multi-year analysis and validation example in Figs. 6 and 7b. (For interpretation of the references to colour in this figure legend, the reader is referred to the web version of this article.)

has also been associated with elevated rates of oak mortality here (e.g., (Das et al., 2020; McLaughlin et al., 2020).

We specifically focus on the ≈1200 km^2 area mapped by the Jepson Flora Project (Baldwin et al., 2020) as *Northern, Central, and Southern Sierra Nevada Foothills: Oak Woodlands*. The ~500 km × 25 km study area ranges in elevation from ~200 to 600 m ASL and is comprised of rolling hills dissected by east-west running canyons. The climate of the study area is classified as hot summer Mediterranean (Köppen *Csa*).

The San Joaquin Experimental Range (SJER), a longstanding research station (est. 1934), is chosen as the location of our LiDAR-based validation/comparison on the basis of extensive ancillary data associated with its status as a Core Terrestrial site of the National Ecological Observatory Network (NEON). *Quercus douglasii* (blue oak) and *Q. wislizeni* (interior live oak) are the dominant oaks here. Herb layer composition is diverse and spatially variable but dominated by Mediterranean annual grasses such as *Avena barbata*, *Bromus diandrus*, *B. hordeaceous*, and *Festuca myuros*, as well as native and non-native annual forbs such as *Lupinus bicolor*, *Erodium cicutarium* and *Medicago polymorpha* (McClaran and Bartolome, 1989). Scattered shrubs include evergreen chaparral species, notably *Ceanothus cuneatus*.

Sequoia National Park (SNP) is a longstanding federally protected area (est. 1890). Most of the park is characterized by rugged topography, with an elevation gradient spanning over 4000 m. A diverse set of vegetation communities exist in the park. We focus on the relatively small spatial subset of SNP which hosts blue oak woodlands, found at low elevations near the western park boundary. These woodlands are dominated by *Q. douglasii*, and also commonly include *Q. wislizeni*, *Aesculus californica* (California buckeye) and *Fraxinus dipetala* (California ash). This area was the subject of a recent study by (Das et al., 2020) which presented field evidence of drought-associated oak mortality. We focus our multi-year demonstration in this region.

2.2. The mixed pixel

The combination of discontinuous tree canopy and strongly contrasting herb and soil makes oak woodland spectral properties highly sensitive to sensor spatial resolution (Franklin et al., 1991). Most individual tree crowns are < 10 m in diameter and therefore fall below the scale of the Sentinel-2 and Landsat-series sensors. Because the spatial scale of the objects of interest on the landscape is finer than the spatial resolution of the sensor, most pixels in these images are spatially mixed – i.e., they integrate signal from more than one object on the landscape. This phenomenon is illustrated in Fig. 2. While the 30 cm resolution of the airphoto is sufficient to resolve all individual trees and most shrubs, the area integrated by most Landsat and Sentinel-2 pixels (gray squares) clearly extends beyond individual canopies. The mixed pixel is thus a fundamental characteristic of decameter resolution imagery of the Sierra foothills (and many other landscapes), suggesting the applicability of L-resolution models – and intrinsic limitations of H-resolution models – as described by (Strahler et al., 1986). Spectral and temporal mixture models take just such an L-resolution approach by fundamentally acknowledging that the objects of interest are finer than the scale of the pixel and treating this subpixel heterogeneity in an explicit and transparent way.

Spectral mixture analysis (SMA; Adams et al., 1986; Gillespie, 1990; Settle and Drake, 1993) is one well-understood approach to the mixed pixel problem for single image acquisitions. SMA optimizes the extraction of information from a multispectral image by considering the radiance (or reflectance) measured by each pixel as a linear combination of the radiance (or reflectance) of spectral endmember materials, plus error. The areal cover of each endmember within the spatial extent of each pixel can then be estimated accurately using least squares. The subpixel areal abundances of each EM are estimated through the inversion of a system of linear equations of the form:

$$f_S E_{S,\lambda_i} + f_V E_{V,\lambda_i} + f_D E_{D,\lambda_i} + \varepsilon = R_{\lambda_i}$$

Where $R_{\lambda i}$ is the observed reflectance at a given wavelength; f_S, f_V, f_D are the fractional subpixel area cover of the Substrate (S), Vegetation (V) and Dark (D) EMs; $E_{S,\lambda i}$, $E_{V,\lambda i}$, $E_{D,\lambda i}$ are the reflectances of the S, V and D EMs at each wavelength; $\lambda_i \in$ {482 nm; 561 nm; 655 nm; 865 nm; 1609 nm; 2201 nm} (in the instance of unmixing with bands 2–7 of Landsat 8 OLI), and ε is model misfit, respectively.

A fundamental assumption of spectral mixture analysis is that the landscape is comprised of a *small number of materials with distinct*

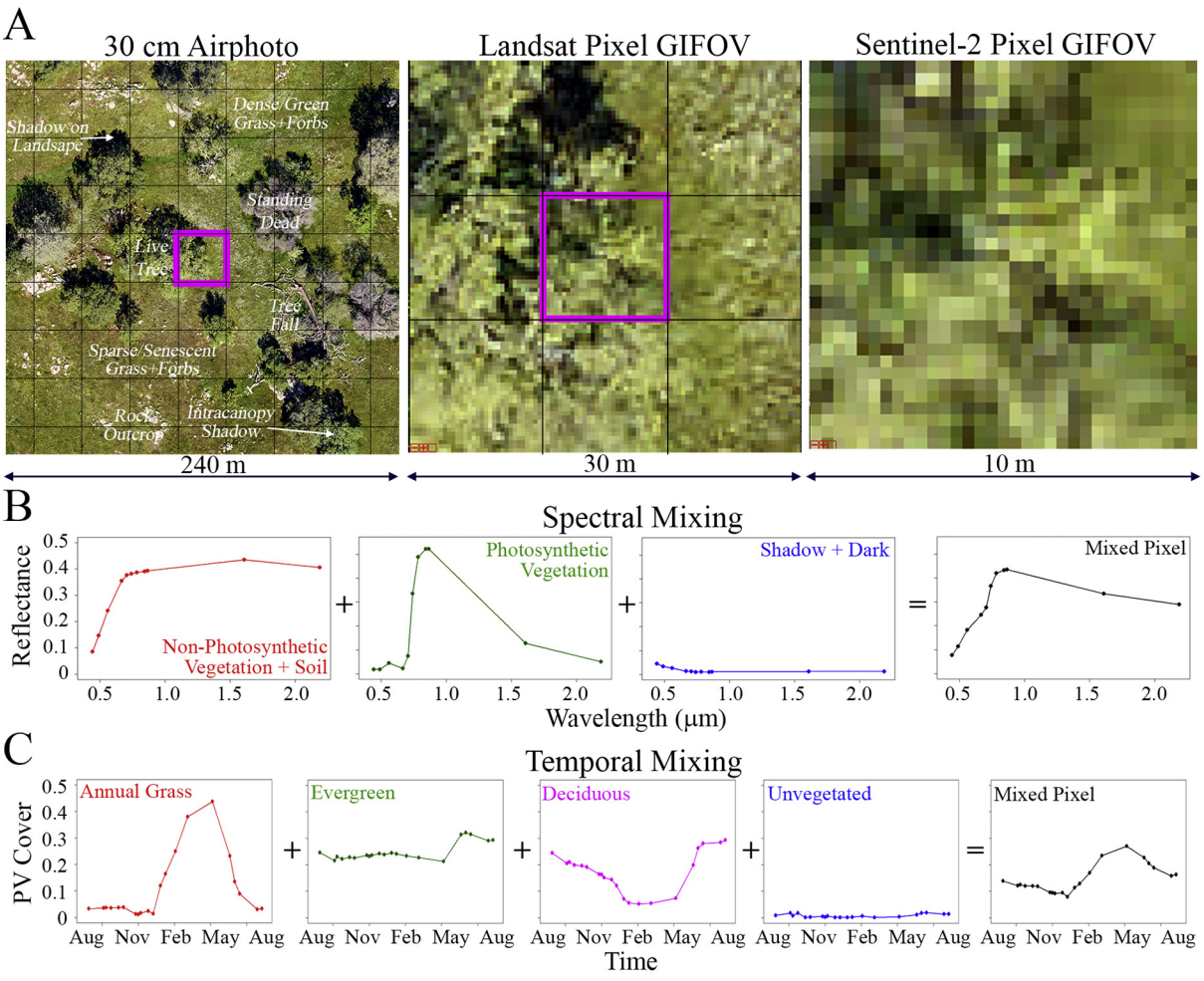

Fig. 2. Subpixel mixing. A. Oak woodlands and savannas are spatially undersampled by decameter resolution sensors like Landsat and Sentinel-2. Example shown for an area within the San Joaquin Experimental Range (SJER). At 30 cm airphoto resolution (left), the landscape can be profitably segmented into discrete objects - and their shadows. At the scale of 30 m Landsat/HLS and 10 m Sentinel-2 VNIR image time series, however, most pixels are comprised of varying mixtures of biotic and abiotic materials. B. Spectral mixture modeling estimates area abundance of spectrally distinct endmember materials within each mixed pixel. C. Temporal mixture modeling simply extends this concept to the time domain, estimating subpixel area abundance of temporally distinct phenologies or multi-year trajectories.

spectral signatures. Linear mixing is also assumed. This concept is illustrated in Fig. 2b (center row), where the reflectance of an example mixed pixel (black curve on right) is considered to be a weighted sum of the reflectances of constituent spectral endmember reflectances (red, green and blue curves on left). SMA has been shown to accurately estimate vegetation cover, even in sparse and multiple scattering environments like semiarid shrublands (Smith et al., 1990), exceeding the accuracy of spectral indices like NDVI in field validation exercises (Elmore et al., 2000) and not suffering from the well-known issues with NDVI stemming from the impact of soil background and atmospheric effects (Sousa and Small, 2017).

In some cases, the concept of subpixel mixing can be profitably extended to the time domain. Using this approach, a landscape is considered to be comprised of a *small number of "materials" with distinct temporal signatures*. Usually, a single variable is first extracted from each image in the multispectral time series (e.g. subpixel cover of a single material, like photosynthetic vegetation, from SMA; or a spectral index). This reduces the dimensionality of the observation space from (*t x b)* to *t*, where *t* is the number of images in the time series and *b* is the number of spectral bands in each multispectral image. The result of this step is a substantial conceptual simplification and reduction of computational load. Temporal mixing is conceptually illustrated in Fig. 2c (bottom row), where an example vegetation cover time series of a mixed pixel (black curve on right) is considered to be a linear sum of endmember vegetation phenologies (red, green, magenta and blue curves on left). The subpixel areal abundances of each temporal EM can then be estimated through the inversion of a system of linear equations analogous to the spectral mixing equations:

$$f_{tEM1}E_{tEM1,t_i} + f_{tEM2}E_{tEM2,t_i} + f_{tEM3}E_{tEM3,t_i} + \ldots + f_{tEMn}E_{tEMn,t_i} + \varepsilon = V_{t_i}$$

Where V_{ti} is the SMA-estimated vegetation cover at a given time; f_{tEM1}, f_{tEM2}, f_{tEM3}, … f_{tEMn} are the fractional subpixel area cover of the 1st, 2nd, 3rd, … nth temporal endmembers; $E_{tEM1,ti}$, $E_{tEM2,ti}$, $E_{tEM3,ti}$, … $E_{tEMn,ti}$ are the vegetation cover values of the 1st, 2nd, 3rd, … nth temporal endmembers at each time step t_i; $t_i \in$ {1st image date, 2nd image date, 3rd image date, … last image date}, and ε is model misfit respectively.

Notably, the temporal mixing approach is fundamentally different from statistical approaches to multitemporal analysis of the land cover fractions derived from SMA because it treats the pixel time series as area-weighted fractions of constituent temporal patterns. Many studies have used SMA to generate inputs to further multitemporal statistical analyses, such as using vegetation cover as the basis of logistic phenology models (Fisher et al., 2006) or Tasseled Cap brightness/greenness/wetness as inputs to multitemporal unsupervised classifications of land cover (Kuemmerle et al., 2006). However, far fewer have used SMA fraction estimates as the basis for temporal mixture models (e.g. Small, 2012; Sousa and Small, 2019). This temporal mixing approach is

investigated in the present analysis.

Obviously, the implementation of temporal mixture analysis is considerably less straightforward than spectral mixture analysis. A number of stringent data quality and standardization requirements must be met in order for this approach to be tractable: e.g. subpixel coregistration, radiometric calibration, and consistent atmospheric correction. In addition, the formulation of the temporal mixing inverse problem is generally less well-posed than the spectral mixing inverse problem because biogeophysical parameters (e.g. vegetation cover) can change with time in many more ways than reflectance can change with wavelength. Potential impacts of this complexity include a much higher dimensional feature space and more poorly conditioned endmember matrix for the temporal case than the spectral case. Adding to this complexity, variations in illumination and viewing geometry can introduce systematic artifacts which confound straightforward interpretation, particularly in savannas where tall trees with voluminous canopies can cast laterally extensive and seasonally variable shadows (Franklin et al., 1991). Topography also compounds these effects. However, while these challenges complicate temporal mixture analysis, they also impact any method for satellite image time series analysis. Fortunately, decades of effort in development and implementation of preprocessing routines has succeeded in mitigating – albeit never truly eliminating – the most severe of these complications.

Furthermore, the single- and multi-year temporal mixing cases are characterized by important conceptual differences. The product of the single-year unmixing problem is essentially a phenology map. Single-year temporal endmembers generally correspond to plants with varying annual cycles in leaf area and primary productivity. Considering a pixel time series to be a linear mixture of areal cover of plants with varying phenologies is bears clear conceptual similarities to the spectral mixing problem. However, the application of temporal mixture modeling to multi-year time series is more complex, and in many cases may not provide a reasonable representation of the ecological dynamics at play. The critical confounding factor is the potentially immense number of life histories of individual trees and shrubs, occurring at varying rates and with varying start times. If this range of trajectories is too large or complex to be represented by a relatively small number of temporal endmembers, a simple mixing model is unlikely to yield satisfactory results.

However, in the case of Mediterranean systems, ecoclimatic shocks often occur synchronously across large swaths of landscapes (e.g. drought, spatially extensive wildfires). In these cases, it is plausible that the complex life history space of the landscape may collapse onto a small number of trajectories with similar initiation times. If the ecological purpose of the analysis is to detect and quantify spatiotemporal patterns of change associated with the event, these trajectories may provide sufficient information to make the approach profitable. The conceptual model of spatial mixing still holds because an individual 30 × 30 m Landsat pixel could easily be comprised of individual trees and shrubs with disparate levels of impact (e.g. 1 deciduous oak strongly impacted by drought; 1 evergreen oak unimpacted by drought; several young and growing shrubs; ….). We examine whether multi-year vegetation trajectories exhibit generally synchronous response to severe drought by examining model outputs in an area with field documented oak decline in Sequoia National Park (Das et al., 2020). While temporal mixture modeling is clearly not the only approach that can be taken to this problem (McLaughlin et al., 2020), the relative novelty and conceptual simplicity of the method make the application to tree mortality monitoring worth examining.

3. Materials and methods

3.1. Single-year phenology mapping

The single-year (phenology) portion of the analysis was based on the time period July 1, 2018 through July 1, 2019. The Harmonized Landsat-Sentinel (HLS) S30 data product was the source of 30 m data, downloaded from: https://hls.gsfc.nasa.gov/. HLS data are produced free of charge and have undergone standardized radiometric, atmospheric, terrain, and BRDF correction. All available HLS images for tiles 10SFH, 10SFJ, 10SGH, 11SKA, 11SKB, 11SLA and 11SLV over the study period were downloaded and visually inspected. Images with visible cloud cover and swath edge images with partial spatial coverage were removed. Linear spectral mixture analysis was then performed on each remaining image based on standardized global spectral endmembers from (Small, 2018). These endmember spectra are qualitatively similar to previously published Landsat 7 and 8 endmembers from global analyses (Small, 2004; Small and Milesi, 2013; Sousa and Small, 2017), as well as Landsat 8 and AVIRIS endmembers from coincident acquisitions in spatially constrained but spectrally diverse California landscapes (Sousa and Small, 2018). A unit sum constraint with a weight of unity was used for all instances of spectral and temporal mixture analysis. This approach has proven satisfactory for the spectral mixing case in previous studies (Small, 2003; Small, 2001; Sousa and Small, 2017). For the temporal mixing cases, varying unit sum constraint weights were compared for the tiles containing the SJER and SNP validation areas, including unconstrained models. Results did not change appreciably with varying weights, and RMS misfits were low (e.g. 97% of pixels with RMSE < 0.05 for the single-year TMM), so the same unit sum weight (1) was used in all unmixing cases for consistency. Shade/dark normalization was also investigated for these two tiles. Upon shade normalization, however, the geometric configuration of the TFS was partially collapsed, endmember clarity was reduced, and resulting TMM maps were noisier than those estimated without applying the additional normalization step. We suspect that this may be because 1) dark fraction can provide information about subpixel vegetation structure which is a source of signal for the TMM, and 2) we do not have sufficient information to accurately partition shade/dark fractional area into substrate vs vegetation cover. We acknowledge shade/dark normalization can be appropriate in some circumstances, but do not apply it throughout this analysis for these reasons. The vegetation cover images were stacked to produce a single image time series for each tile. The images used for each tile are listed in Table S1. The single-year 30 m stacks were used for PhenoCam comparison (Fig. 4), single-year example TMM (Fig. 5), and investigations of spatial scaling (Fig. 8), temporal aliasing (Fig. 9), and cross-tile consistency (Fig. 10).

10 m maps used for LiDAR comparison (Fig. 7a) and spatial scaling (Fig. 8) were derived from Sentinel-2 data downloaded free of charge from the Copernicus data portal: https://scihub.copernicus.eu/dhus/. Images were downloaded as Level 1C Top of Atmosphere (TOA) reflectance and processed to Level 2 Surface Reflectance using the Sen2Cor processing module available within the ESA SNAP freeware program. 20 m bands were resampled to 10 m resolution. Surface reflectance images were then unmixed to produce subpixel vegetation cover estimates using the same globally standardized spectral endmembers referenced above. Only tile 11SKB (encompassing the SJER field site) was used for the 10 m maps. The same image dates (Table S1) were used to make the 10 m and 30 m single-year stacks.

3.2. Multi-year change mapping

The multi-year portion of the analysis was based on the time period from August 2000 through August 2019. Thirty meter resolution maps for the multi-year analysis were derived from Landsat 5 and 8 imagery, viewed at: https://glovis.usgs.gov/. All available August images from Path 42, Row 35 were visually examined. Level-2 surface reflectance images for all visibly cloud-free acquisitions were ordered from EarthExplorer (https://earthexplorer.usgs.gov/) and downloaded from the ESPA download hub (https://espa.cr.usgs.gov/). Although the sidelap of Path 41, Row 35 also includes much of Sequoia National Park, this tile was not included in the analysis to minimize BRDF-related uncertainty and because spatial coverage of the oak landscapes of

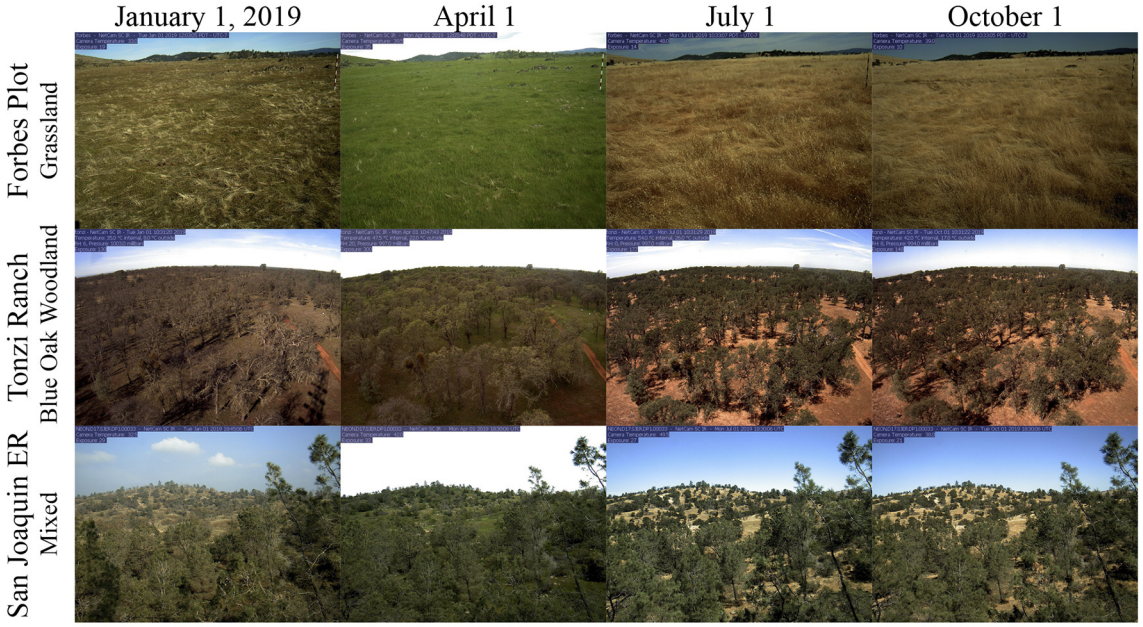

Fig. 3. PhenoCam field photos. Oak density in Sierra foothill landscapes grades continuously from open, nearly treeless grasslands to closed canopy woodlands. The PhenoCam network captures sites which span much of this range. Spatially averaged phenology of open grasslands (Forbes Plot at Sierra Foothill Experimental Range) is visibly different from oak-dominated woodlands (Tonzi Ranch). Evergreen in the mixed landscape of the San Joaquin Experimental Range have yet different phenology. Annual cycles for each location are shown using mid-day images. In areas dominated by annual grasses and deciduous oaks, maximum vegetation cover (and primary production) occurs in the spring, when temperatures warm and root zone water content is greatest. Non-native grasses senesce rapidly in late spring, but oaks (as well as some grasses, forbs, and shrubs) generally remain green through fall. (For interpretation of the references to colour in this figure legend, the reader is referred to the web version of this article.)

interest is incomplete. August was chosen to optimize viewing & illumination geometry, maximize the probability that healthy winter-deciduous blue oaks would be leaf-on, and minimize the probability that summer-deciduous trees like the California Buckeye would be leaf-on. Linear spectral mixture analysis was then performed on each image based on cross-calibrated global spectral endmembers from (Sousa and Small, 2017). A unit sum constraint with a weight of unity was again used for all instances of spectral and temporal mixture analysis. The vegetation cover images were stacked to produce a single multi-year image time series and used for the SNP analysis (Fig. 6). The images used are listed in Table S2.

3.3. Ancillary field and airborne observations

PhenoCam data were downloaded free of charge from the PhenoCam webpage: https://phenocam.sr.unh.edu/. Plots were made using 3-day maximum midday green chromatic coordinate (GCC) and standard regions of interest available on the PhenoCam website. The SJER top-of-tower PhenoCam was repositioned partway through the time series, so only images from after the repositioning (September 28, 2018 onward) were used.

The NEON Airborne Observation Platform (AOP) collected 30 cm resolution orthophotos and LiDAR at the SJER site in June 2013, and March/April 2017, 2018, and 2019. These data were downloaded free of charge from the NEON data portal (https://data.neonscience.org/home). The 1 m 2018 LiDAR canopy height model (CHM) was converted to tree presence/absence by simple thresholding. A number of thresholds were tested, and a conservative 3 m threshold was ultimately adopted. The 1 m image was then aggregated to 10 m resolution and convolved with a 9 × 9 pixel low-pass Gaussian blurring filter to approximate the point spread function of Sentinel-2 sensor. Because both the “deciduous perennial” and “evergreen perennial” endmembers are associated with trees and shrubs, these two cover fractions were summed to form a “tree” cover estimate in the single-year dataset.

Unfortunately, healthy leaf-off deciduous oaks could not be confidently discriminated from defoliated/standing dead oaks in the 2017, 2018 and 2019 NEON AOP airphotos due to flight timing (late March to early April) occurring prior to full greenup of deciduous oaks. Validation of the single-year TMM was done by comparison to the 2018 and 2019 NEON AOP (to discriminate among grasslands, evergreen trees, and deciduous/dead trees), then cross-checked against orthophotos and meter-resolution satellite imagery available on Google Earth. Validation of the multi-year TMM was done by comparison to Google Earth imagery alone. Availability of summer validation images at SNP were limited (single image pair from 6/27/2010 and 5/31/2014), not allowing for confident assessment of the early decline + revegetation endmember fraction.

4. Results

Results are presented in the following sequence. First, we leverage the PhenoCam sites to visually display the field-based time varying optical properties of representative landscapes in the study area, qualitatively connect satellite image time series to ground-based phenology observations, and compare quantitative field-based and satellite-based metrics (Subsection A). Next, we present an illustrative example of the workflow of characterization and modeling (B), followed by validation and comparison (C) of both single-year phenology mapping and multi-year change mapping. We then examine the sensitivity (D) of the resulting maps to pixel size, temporal sampling, and spatial consistency across the Sierra foothill spatial domain.

4.1. Relating ground and satellite observations

Initial characterization is performed using time lapse field photography from the PhenoCam program (locations shown in Fig. 1). These images provide useful qualitative and quantitative information for relating time-varying surface biophysical properties to satellite image time series (Fig. 3). Sites include a spatially extensive annual grassland (Forbes Plot at the Sierra Foothill Experimental Range), a deciduous

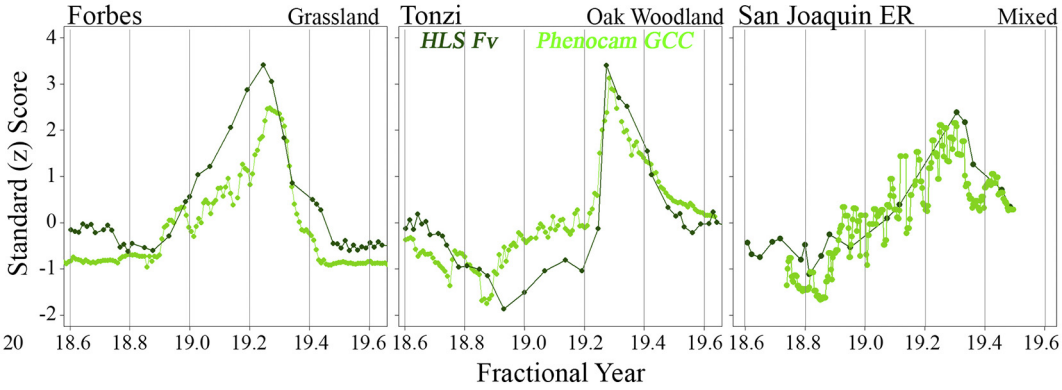

Fig. 4. Phenocam versus satellite time series for the 2018–2019 water year. Forbes grassland (left), Tonzi Ranch blue oak woodland (center) and San Joaquin Experimental Range (right) are compared. 3-day average Green Chromatic Coordinate (GCC; lighter curve) from standard PhenoCam regions of interest is compared with Harmonized Landsat-Sentinel (HLS) estimates of illuminated photosynthetic vegetation cover (Fv) from the pixels nearest the viewshed of each PhenoCam. For comparison, time series are normalized by transformation into Standard (z) Scores [i.e. (x-m)/s]. Grasses show gradual greenup throughout winter followed by abrupt late spring senescence. Blue oak woodlands show leaf loss in late fall/early winter and remain defoliated until spring. Mixed landscape at SJER has a less distinct phenology signal. The level of PhenoCam/HLS agreement (correlations in the 0.8 to 0.9 range) is encouraging given differences in spatial coverage, sensing modalities and view angle. Differences are likely due to a combination of BRDF effects and nonlinearities between the GCC and Fv metrics. The spectral mixture model also produces simultaneous estimates of two other land cover fractions (Substrate and Dark). Correlation between the Substrate fraction and PhenoCam Red Chromatic Coordinate (RCC) time series (not shown, 0.75 to 0.9) is also encouraging. (For interpretation of the references to colour in this figure legend, the reader is referred to the web version of this article.)

blue oak woodland (Tonzi Ranch), and a mixed grassland/evergreen oak/deciduous oak/conifer landscape (SJER) (Fig. 3).

Strong seasonality in photosynthetic vegetation cover is readily apparent at each location, but with plant types differing widely in amplitude and rate. Spatially averaged estimates for each location are shown using both ground-based and satellite-based metrics in Fig. 4. Because of the differences in GCC and Fv metrics used across sensors (detailed in Materials and Methods), each plot is converted into standard scores (z-scores) by subtracting data values by the time series mean and dividing by the standard deviation. Correlation coefficients of ground-based and satellite-based time series range from 0.8 to 0.9.

Clear differences in amplitude and timing exist among the three sites. The grass-dominated, northernmost Forbes site shows a gradual green-up throughout the winter as grass growth is enabled by winter precipitation but rate-limited by cold winter temperatures. Following the peak in early spring, the grasses senesce rapidly as water becomes limited, with a brief plateau in late spring/early summer. The blue oak woodland at the Tonzi site shows a rapid green-up in late spring as grass growth coincides with abrupt leaf-on of the deciduous oak canopy. Senescence also begins rapidly as the grass understory dries, but then slows and continues throughout the summer and into late fall/early winter, as the chlorophylls in blue oak leaves slowly degrade over the course of several months. Deciduous blue oak leaves then fall to the ground, resulting in an abrupt drop in greenness toward the end of the calendar year. Finally, the temporal signature of vegetation cover in the mixed landscape at SJER shows less pronounced seasonality as a result of a greater cover of evergreen oaks and conifers.

In short, the three exemplary PhenoCam sites illustrate three distinct phenologies present in the Sierra foothill oak woodland study area – annual grasses at Forbes; deciduous trees and shrubs at Tonzi; and a mixture including evergreen trees and shrubs at SJER. These phenologies can be quantified with comparable fidelity using both ground-based and satellite-based metrics. This context is invaluable for TMM implementation and interpretation, presented next.

4.2. Spatiotemporal characterization & temporal mixture modeling

The following methodology is based in two stages: 1) *characterization* of the dominant spatiotemporal patterns present in the image time series, and 2) *modeling* the data as a linear combination of these endmember patterns. Characterization consists of Empirical Orthogonal Function (EOF) analysis of the image time series, followed by interrogation of the associated Temporal Feature Space (TFS) to find bounding temporal endmembers (tEMs) as described by (Small, 2012). Modeling is performed by least squares. For the sake of brevity, we omit detailed discussion of the partition of variance, covariability matrices, and higher order dimensions in the current analysis. Instead we focus on the geometric structure of the low-order (Dimensions 1–3) projections of the TFS. We also focus the following portion of the analysis (Figs. 5-9) on single tile spatial domains, deferring extension of the results to the remainder of the study area until Fig. 10. In order to illustrate the range of potential uses of the method, both single-year and multi-year use cases are investigated.

4.2.1. Single-year

We begin by applying a covariance-based Principal Components transform to the single-year time series. The associated low-order TFS with bounding tEM phenology time series (left) and TMM phenology map (right) are shown in Fig. 5. The single-year vegetation cover image time series is characterized by four distinct tEM phenologies located in clearly defined corners of the low-order temporal feature space: annual grasses (Ag), deciduous perennials + seasonal shadow (D), evergreen perennials (E), and unvegetated surfaces (U). Importantly, the annual cycle of subpixel photosynthetic vegetation for deciduous trees and shrubs is mimicked by the annual cycle of shadowing. This fundamental ambiguity reduces the accuracy of the deciduous cover estimate. The choice of Ag, D, and E single-year endmembers from the HLS spatiotemporal characterization is further reinforced by clear correspondence to the PhenoCam time series (Fig. 3).

The Ag, D, E and U tEMs bound a roughly tetrahedral mixing space, illustrated by the white lines drawn on the TFS for conceptual guidance. The TMM constructed from these tEMs represents the vegetation time series of each pixel as a linear combination of the constituent tEM phenologies. The contribution of each tEM to a pixel time series can be visualized as the Euclidean distance of that pixel from the corner of the tetrahedron corresponding to each tEM.

When displayed in geographic space, the relative contribution of each tEM generates a phenology map. This map represents the Sierra foothill landscape within tile 11SKB in terms of subpixel spatial cover of deciduous perennials (red), evergreen perennials (green) and annual grasses (blue). Plant communities with homogenous phenologies are represented by the additive primary colors. Plant communities with

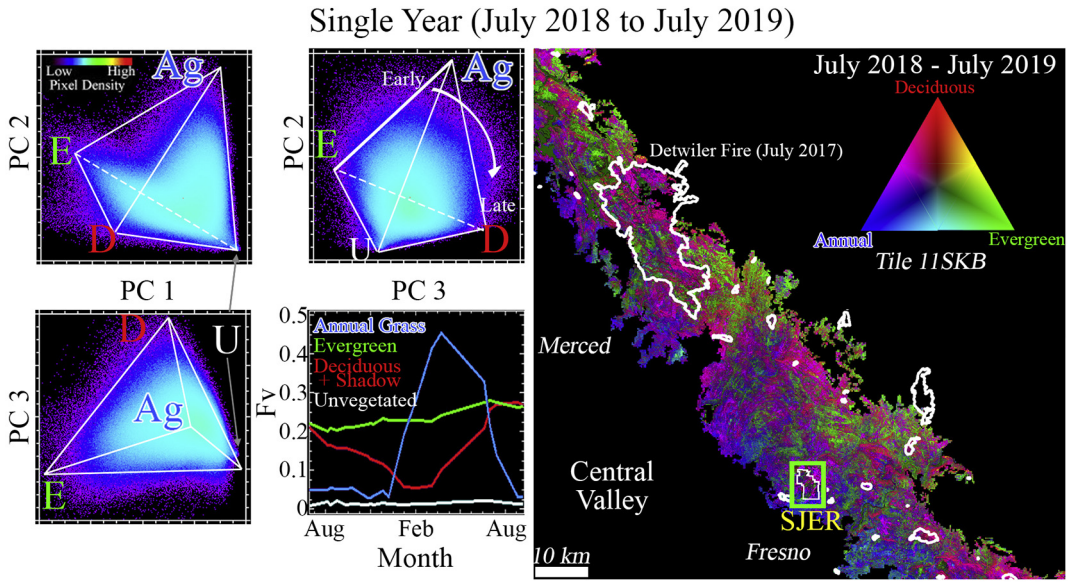

Fig. 5. Single year example. The temporal feature space (TFS; left) and associated temporal mixture model (TMM; right) map are illustrated using a single year time series of vegetation abundance in tile 11SKB. The first three dimensions of the single year TFS clearly allow for discrimination between annual grasses (Ag), deciduous perennials + seasonal shadow (D), evergreen perennials (E), and unvegetated areas (U). Temporal endmembers (tEMs) representing each phenology are selected from the corners of the TFS and plotted in the lower right quadrant. These tEMs are then used to unmix the vegetation time series, generating a phenology map. The area surrounding San Joaquin Experimental Range (J; green box) is used for LiDAR comparison in Fig. 7a. Fire perimeters (2015 onward) shown by white vectors. (For interpretation of the references to colour in this figure legend, the reader is referred to the web version of this article.)

intermixed phenologies correspond to areally weighted color combinations of the additive primaries. As noted above, the deciduous signal is mimicked by seasonal shadow. Despite this fundamental ambiguity, the overall spatial pattern associated with the single-year TMM is consistent with well-documented vegetation gradients over the region. The validation location (Section C) is indicated by the green box.

4.2.2. Multi-year

Another approach to analysis focuses on multi-year change rather than single-year phenology. To illustrate this analogous approach, we use the 2000–2019 August image time series of Sequoia National Park. This time period was chosen to span the duration of the historic 2012–2016 drought (Flint et al., 2018) as well as provide over 10 years preceding the event to understand the pre-drought baseline. The corresponding TFS with bounding tEM multi-year trajectories (left) and

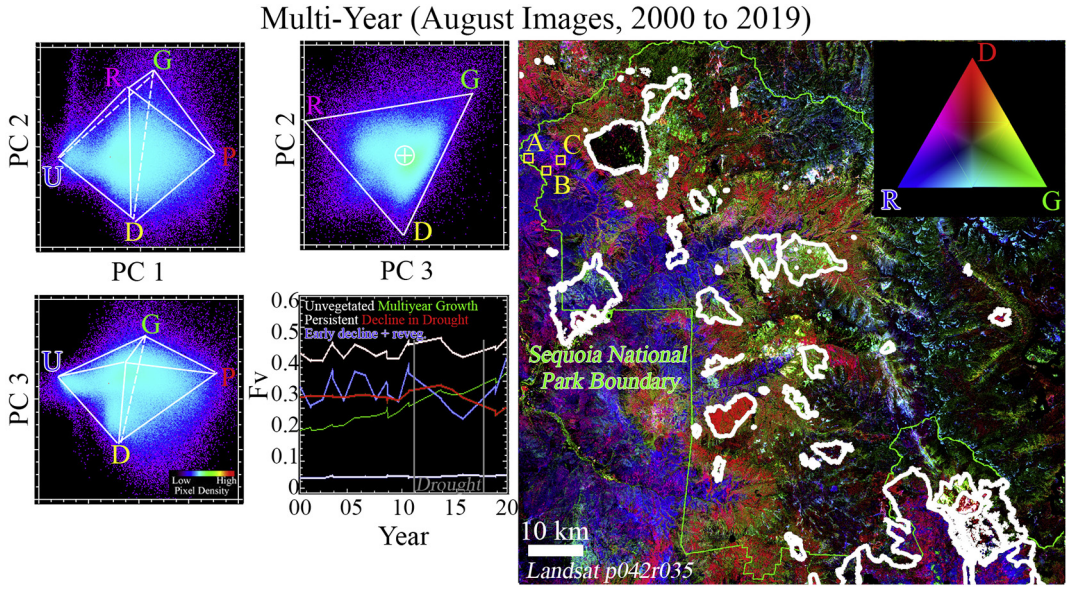

Fig. 6. Multi-year example. TFS (left) and associated TMM map (right) show a multi-year change analog to the single-year phenology example from Fig. 5. Model is based on a 20-year Landsat 5 and 8 time series of August vegetation cover for Sequoia National Park and environs. Locations of example validation sites (A, B & C) shown in Fig. 7b are indicated with yellow boxes. The low-order TFS forms a mixing space approximating a trigonal dihedral geometry, outlined by white lines. Temporal endmembers correspond to unvegetated (U; white), persistent (P; white), multiyear growth (G; green), decline during 2011–2017 drought (D; red), and decline in early years of drought followed by regrowth (R; blue). Beginning and ending of drought indicated by vertical gray lines. TMM shows spatial patterns corresponding to the R, D, and G tEMs. Park boundary shown with green vector and fire boundaries (1990-present) shown with white vectors. (For interpretation of the references to colour in this figure legend, the reader is referred to the web version of this article.)

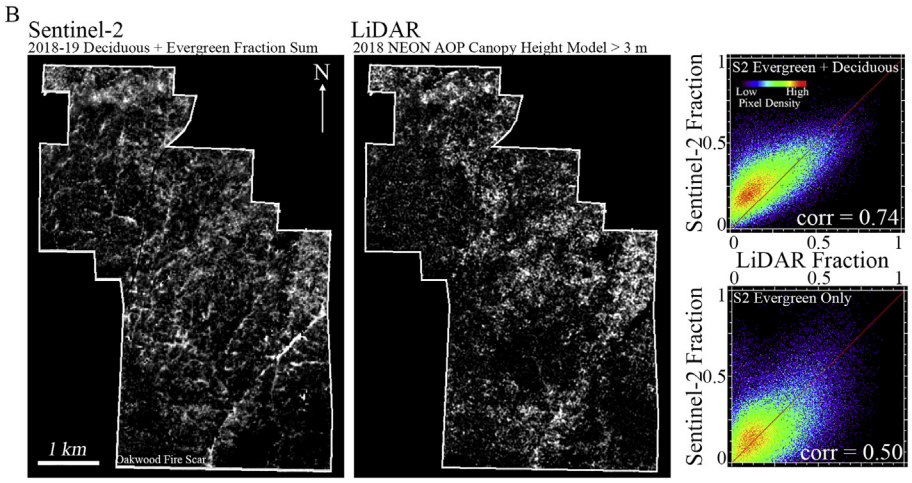

Fig. 7. (a) Comparison of tree cover estimate to SJER LiDAR. Sentinel-2 single year evergreen + deciduous fraction sum correlates with 2018 NEON AOP LiDAR canopy height model > 3 m at a level of 0.74. Sentinel-2 fractions slightly overestimate tree abundance at low fractions and underestimate tree abundance at high fractions. Correlation is substantially weaker for Sentinel-2 evergreen or deciduous fraction alone, as expected given mixed tree phenology. (b) Example multi-year validation. Visual comparison of meter-resolution imagery for locations indicated as decreasing through the drought. Image availability is limited, requiring the use of early summer (late May and late June) images. Despite this limitation, clear evidence of browning/defoliation is observed in 31 of the 34 areas indicated by the TMM as > 0.9 fraction of the Decrease temporal endmember. These results agree with the field measurements of (Das et al., 2020) and provide additional context in the form of spatial and temporal constraints on canopy loss.

TMM multi-year change map (right) are shown in Fig. 6. A number of fires occurred in the area over the duration of the time series. Fire perimeters are shown as white vectors.

In this case, the spatial structure of the TFS is characterized by additional complexity. Endmembers corresponding to multi-year growth (G), decline during the drought years (D) and early decline followed by revegetation (R) are observed, as well as tEMs representing unvegetated locations (U) and locations which maintained persistent August vegetation cover throughout the drought (P). Again, the TMM bounds the mixing space defined by each tEM, in this case forming a roughly trigonal dipyramidal structure (white lines).

The spatial pattern of vegetation response to drought suggests a number of hypotheses regarding the relationship between drought stress and topography. Detailed examination of landscape-scale patterns of drought response is beyond the scope of this work, but some potential paths for future work are further elaborated in the Discussion. The locations of example meter-scale validation images (Fig. 7b) are shown by yellow boxes (A-C).

4.3. Comparison & validation

Comparison of the single-year TMM to the 2018 NEON AOP LiDAR dataset from SJER is shown in Fig. 7a. The spatial extent of the validation corresponds to the area shown in the green box in Fig. 5. The resulting correlation between the Sentinel-2 derived TMM and the LiDAR-derived tree map is 0.74. The strength of the relationship is significantly improved by using the deciduous/shadow + evergreen cover sum described in the Materials & Methods section (upper right) as opposed to a single endmember fraction alone (lower right). This is in accord with the mixture of evergreen and deciduous trees and shrubs at the site.

Additional validation of the single-year phenology map was performed at SJER by comparing single-year phenology maps against submeter resolution airphotos and meter-resolution commercial satellite imagery. The continuous TMM was converted to a binary classification by thresholding. Annual grasslands were mapped as > 0.9 Annual tEM cover; evergreen oak woodlands were mapped as > 0.9 Evergreen tEM cover, and deciduous oak woodlands were mapped as > 0.9 Deciduous + Shadow tEM cover. 34 points were randomly selected from each class and manually compared against airphotos. Classification accuracies were highest for the evergreen woodland (88%) class, with the few observed misclassifications (4 of 34) all occurring in grassland/shrubland environments near lakes and/or in swales. Accuracy for the annual grassland (85%) class was comparable, with the misclassifications (5 of 34) occurring in areas with defoliated (likely dead) tree canopies, rock outcrops, or areas with dense deciduous shrub cover. The lowest accuracy was observed for the deciduous oak class (74%). As expected, misclassifications (8 of 34) were primarily located in areas in which topography generated a seasonal shadow signal that mimicked the deciduous vegetation time series. Some misclassifications were also observed in areas with deciduous (non-oak) shrubs, rock outcrops, swales in open grasslands, or near ponds. The associated single-year confusion matrix is shown in Table S3.

Validation of the multi-year change map was more difficult given the paucity of historic summer meter-resolution imagery and relatively constrained spatial extent of the oak woodlands within Sequoia National Park. However, sufficient imagery was available in 2010 and 2014 to provide some constraints on the Landsat based analysis. Again, the continuous TMM was converted into a discrete classification though simple thresholding. Winter deciduous and evergreen systems with no change were mapped using a rule of Persistent Green tEM cover > 0.9. Systems showing decreased August vegetation cover through the 2012–2016 drought were mapped by using a rule of Decrease tEM cover > 0.9. Systems showing systematically increasing August vegetation cover were mapped by using a rule of Decrease tEM cover > 0.9. Systems showing early decline followed by regrowth were unable to be validated due to absence of available summer meter-resolution imagery after 2014. 34 points were randomly selected and manually investigated for each of the three classes investigated. Spatial extent of validation points was confined to the oak woodland portion of the park as mapped by (Das et al., 2020). Classification accuracy was highest for the pixels showing increased and decreased August vegetation cover through the drought, with 91% of pixels identified correctly in each case. The misclassified points showed either no definitive change in the validation image pair or changes clearly associated with anthropogenic activity. Classification accuracy was lower for the pixels showing persistently high August vegetation cover, with 88% of pixels showing no visible change in the validation imagery. The 4 misclassified points all showed anthropogenic landscape modification. The associated multi-year confusion matrix is shown in Table S4. Example validation image

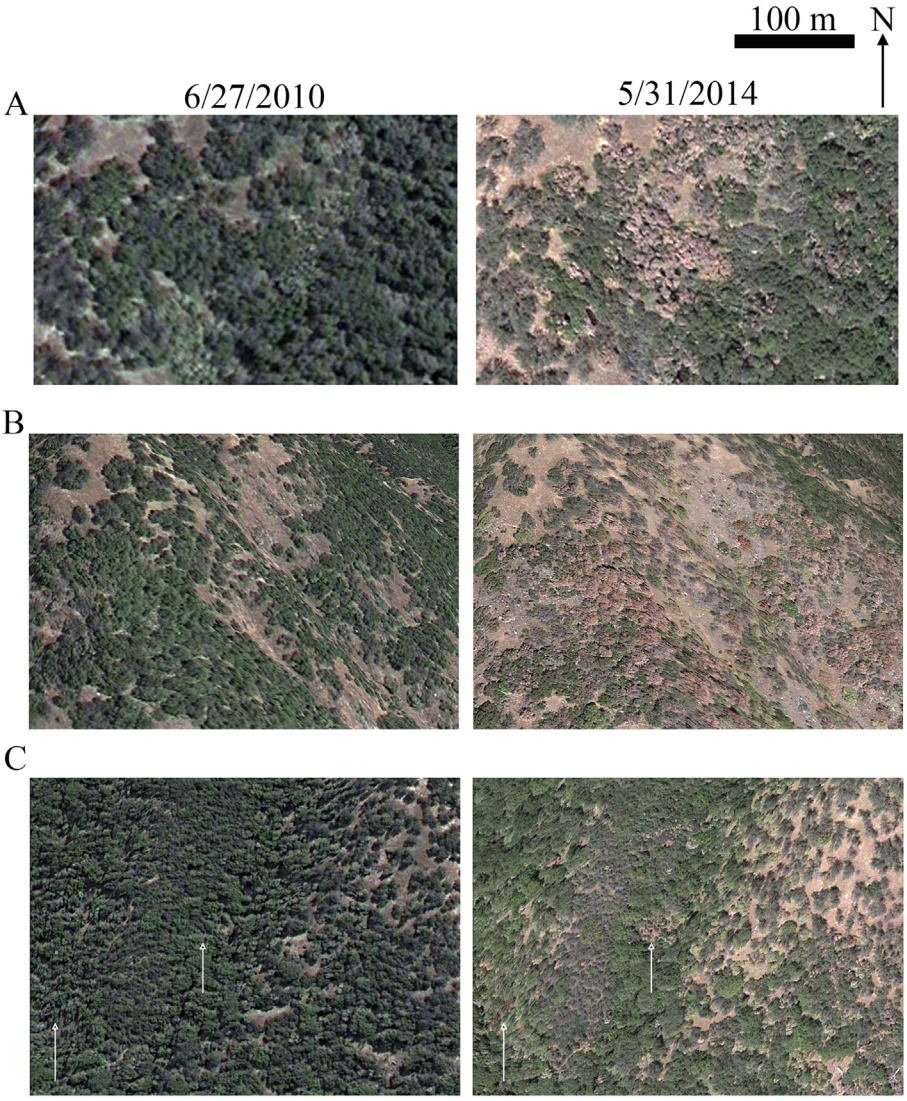

Fig. 7. (*continued*)

pairs for the Decrease endmember are shown in Fig. 7b. Most of the observed canopy browning was found to correspond to spatially contiguous clusters (e.g. panels A and B). In some cases, even browning of individual canopies (e.g. panel C) is detected.

Taken together, the combination of comparison to LiDAR-based tree cover and visual validation of both single-year and multi-year TMMs is encouraging for the potential utility of this for retrospective analysis and prospective monitoring of Mediterranean-climate oak landscapes. However, in order for the results to be maximally generalizable, important questions of sensitivity to spatial resolution, temporal sampling, and sensitivity to spatial domain must be investigated. These factors are considered in the following section.

4.4. Scaling & consistency

We first examine the effect of scaling single-year TMMs from 10 m to 30 m resolution. TFS characterization was done in parallel and tEMs were found to derive from the same pixels in both cases. Each image time series was unmixed using its respective temporal endmembers and cover estimates were compared. Results are shown in Fig. 8. Ten to 30 m scaling of the single-year TMM is generally linear, with best results for deciduous and annual cover estimates (correlations 0.95 and 0.91), and worst results for evergreen (correlation 0.78). Importantly, model misfit also scales linearly and is $< 5\%$ for $> 99\%$ of pixels.

We next investigate the effect of reductions in temporal sampling by systematic decimation, using the single-year 30 m TMM as our example. Fig. 9 shows these results using a range of 24 images/year (full cloud-free HLS time series) down to 3 images/year. The effects on low-order TFS (A), tEMs (B), as well as linearity and bias relative to the full time series (C and D) are documented. While minor differences in the low-order TFS are noticeable in all cases, the geometric structure of the space as well as number and location of bounding tEMs are generally consistent with as few as 4 images per year. Cover estimates show minimal bias or dispersion when subsampling at the 12 image per year level. Nonlinearity is present in the annual cover estimates at 8 images per year, with even more dispersion at 6 images per year but still only minor nonlinearity. Severe nonlinearities and dispersions are observed when sampling is reduced to 4 images per year or fewer.

Finally, we investigate the consistency of the low-order TFS and tEMs across the extent of the study area. Comparable vegetation image time series are constructed for each of the 7 HLS tiles which span the Sierra foothill study area. For consistency, the same number of images in each tile are used, chosen on the basis of atmospheric clarity and maximally evenly spaced temporal sampling. The low-order TFS for each tile is rendered and bounding tEMs are selected. Results for 5 of the 7 tiles are shown in Fig. 10. The two tiles not shown also conform to the pattern and are omitted for display purposes.

The results of the multi-tile experiment confirm that similar low-

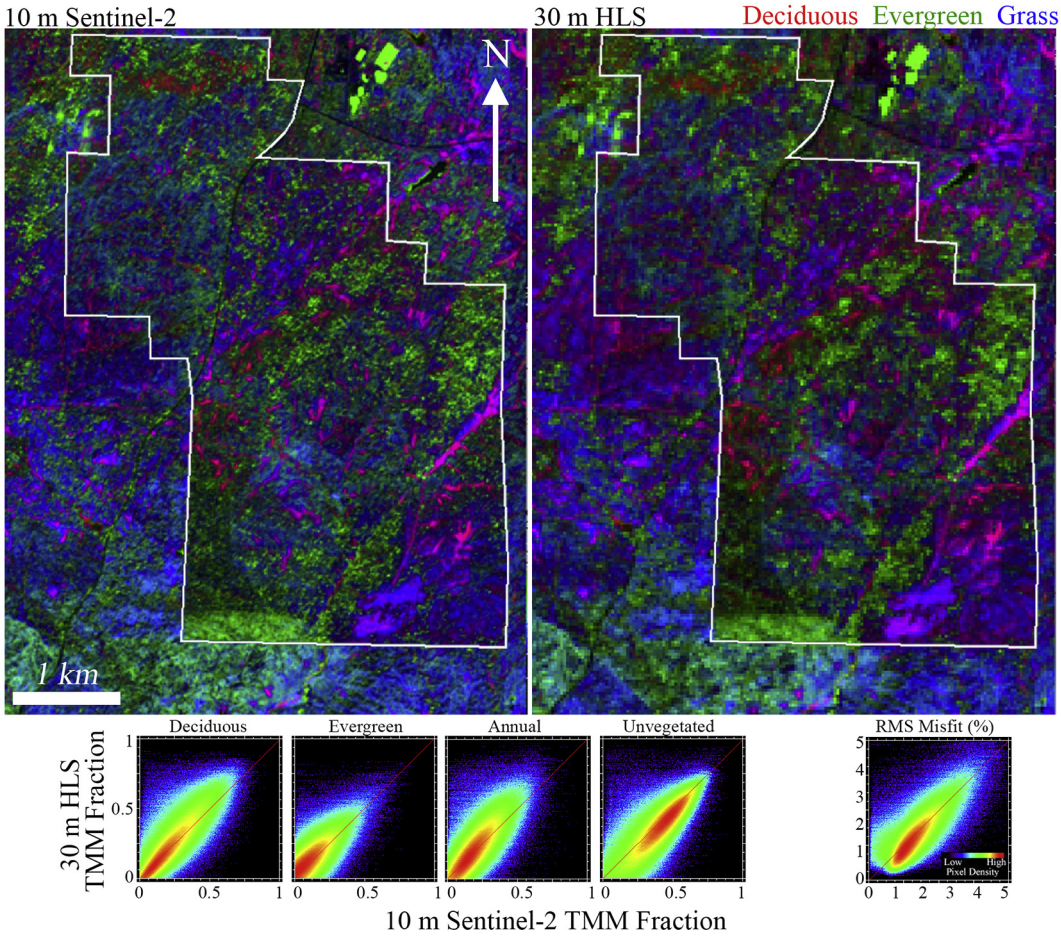

Fig. 8. 10 to 30 m spatial scaling. Temporal mixture model fractions are compared for 10 m Sentinel-2 and 30 m Harmonized Landsat-Sentinel (HLS). Fractions generally scale linearly with correlations between 0.78 and 0.95. Minor bias between datasets is easily correctable with a linear transformation. This suggests that the temporal mixture model approach may be profitably applied for retrospective analysis at Landsat 4–8 spatial resolution.

order TFS geometry and tEMs clearly characterize all but one of the tiles. The tile comprising the exception (11SKA) does not show a clear evergreen tEM. The absence of this tEM is consistent with its relatively minimal spatial extent within the Sierra foothill zone and nearly complete absence of pixels at higher elevations which comprise the bulk of the evergreeen corner of the feature space. The observed consistency in TFS structure, tEM time series, and data dimensionality is taken as further support for the validity of the inferences made in this work across the ≈ 1250 km^2 spatial extent of the Sierra foothill grassland – oak savanna – oak woodland ecosystem.

5. Discussion

5.1. Benefits of the methodology

The methodology presented here possesses a number of benefits for the analysis and monitoring of Mediterranean-climate oak landscapes. Among the primary features are conceptual simplicity, interpretability, and parsimony. These features arise from the linearity of the mixing equations and compact geometric interpretation of the TFS and TMM. By explicitly accommodating the structure of the TFS, the approach is designed such that maximum explanatory power is also retained. Once tEMs are selected, the only tunable parameter is the weight associated with the unit sum constraint.

In addition, the single-year tEMs have clear biophysical interpretation. The phenology signatures present in the PhenoCam time series, HLS time series from single pixels in PhenoCam viewsheds, and independently derived landscape-scale tEMs derived from TFS structure provide mutually reinforcing signals. We interpret this consistency as strong evidence that: 1) the tEMs selected here are stable features of the Sierra foothills spatial domain, 2) the tEMs accurately represent characteristic vegetation phenologies of dominant plant functional types, and 3) multispectral satellite time series of the study area can be well described by these tEMs. We interpret these results as agreeing with previous studies which have favorably compared PhenoCam spectral indices to MODIS/VIIRS spectral indices (Liu et al., 2017; Richardson et al., 2018; Zhang et al., 2018), Landsat/Sentinel-2 spectral indices (Melaas et al., 2016), and Landsat spectral mixture models (Elmore et al., 2012).

At least as important as the features discussed above, however, are the benefits of the robustness and portability of the approach. Supporting observations include linear 10 to 30 m scaling (Fig. 8), insensitivity to (modest) temporal degradation (Fig. 9), and insensitivity to changes in spatial extent across the study domain (Fig. 10). As a further practical consideration, the approach is not computationally onerous (< 1 min unmixing time per tile on laptop computer for 4 EM single-year time series) and does not require extensive training data. These strengths suggest that there is considerable potential for retrospective analysis and prospective monitoring across California foothill oak woodlands. A similar model may also be applicable to biophysically similar Mediterranean-climate oak landscapes in the Mediterranean basin.

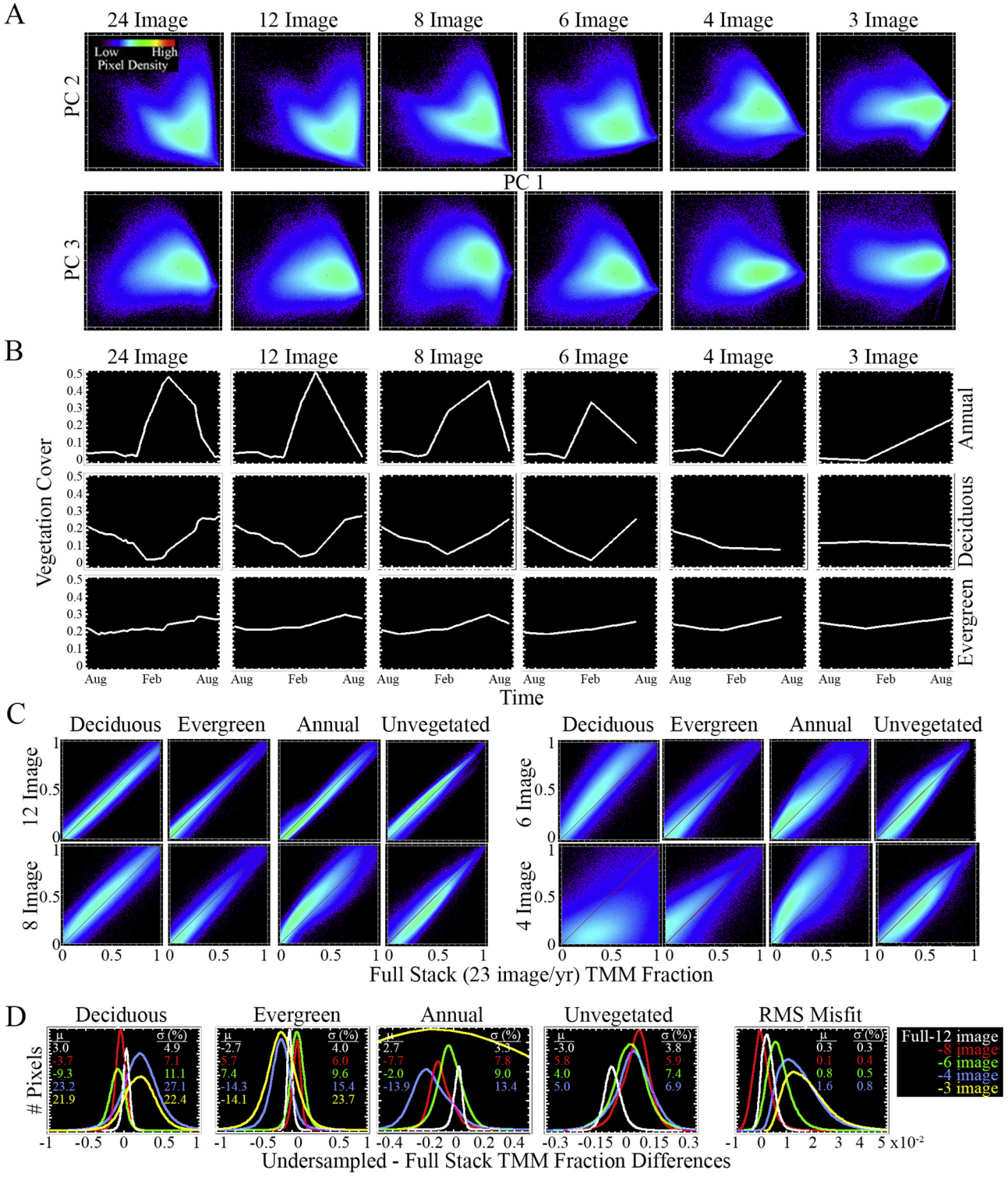

Fig. 9. Temporal aliasing. Effect of degradation of temporal sampling on the single-year temporal feature space (A), temporal endmembers (B), and resulting temporal mixture model fractions (C and D) for the example HLS tile. PC 1 vs 3 topologic relations are generally retained with as few as 6 images. Fraction agreement remains linear down to the 6-image stack. Mean fraction differences are < 10% for each fraction even when the temporal signal is degraded from 24 to 6 images per year. Degradation down to 4- and 3- images per year results in instability in the 4-EM inversion.

5.2. Limitations

Effects due to observational geometry and atmospheric conditions are fundamental limitations that must be considered by all satellite image time series analysis approaches. As noted throughout this analysis, the most prominent way these factor into the model presented here is as potential sources of ambiguity between deciduous vegetation and seasonal shadow. Ongoing improvements in ancillary observations (e.g. digital elevation models, atmospheric constraints) and preprocessing algorithms mitigate the severity of these problems, but are unlikely to ever fully eliminate them – and may introduce additional unintended artifacts. Fortunately, topographic/BRDF effects are relatively minor in

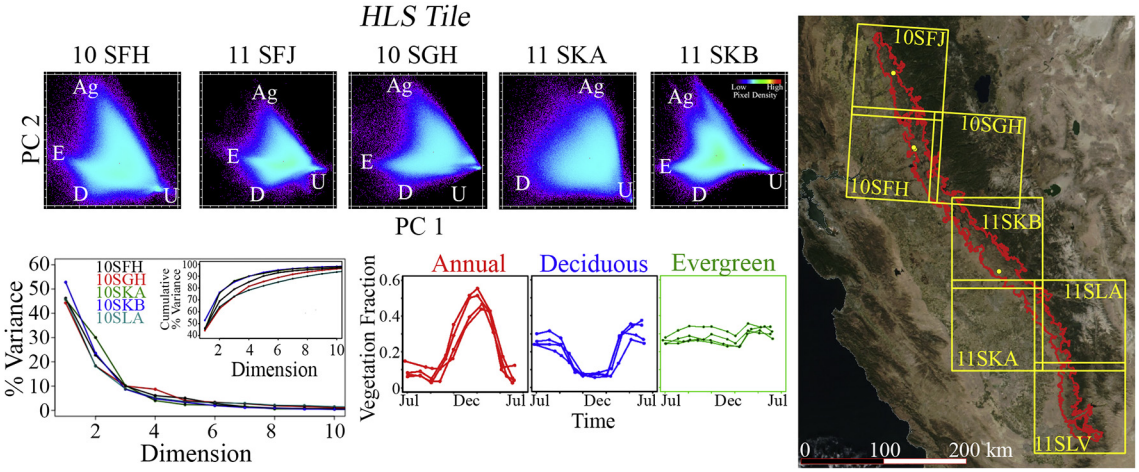

Fig. 10. Cross-tile consistency. Despite spanning hundreds of kilometers, the low-order topology of the foothill oak woodland temporal feature space remains remarkably consistent across HLS tiles. Endmembers located on the PC 1 vs 2 projection represent corresponding phenological signals (evergreen, E; deciduous perennial; D, annual grass, Ag; and unvegetated, U) in each case. The sole exception is tile 11SKA, which does not show an E tEM because its spatial domain within the oak woodland mask does not include sufficient coverage of high elevations. Despite the consistency of the low-order temporal feature space, variation exists in higher dimensions, as revealed by the partition of variance (lower left). For instance, the first 2 dimensions to contain 62–75% of the overall variance in the dataset. The cumulative distribution of variance (inset) also shows this point. In some tiles (e.g. 10SFH), 90% of data variance is contained in the first 4 dimensions; other tiles (e.g. 10SLA) require as many as 10 dimensions to capture 90% of data variance. Tile 11SLA and 11SLV are not shown for brevity.

the Sierra foothills due to moderate topography – but are likely to be more severe in more rugged oak woodland landscapes in California as well as for other ecosystem types. Data loss during times of spatially extensive cloud cover (e.g. winter in the Sierra foothills) remains an unavoidable limitation. This is particularly problematic for retrospective studies which are not able to leverage recent advances capability with respect to shortened revisit time.

Phenology-based studies relying on vegetation cover (or any "greenness" metric) are fundamentally limited by the phenomenon of "phenological mimicking", analogous to spectral mimicking (Adams and Gillespie, 2006). Because the operative signal is derived from temporal variations in photosynthetic vegetation, in many landscapes it is probable that several dominant plant species may possess annual cycles that are indistinct using this metric alone. Careful consideration of sources of uncertainty as well as field validation (wherever possible) is important here as in any mapping and modeling approach based on multispectral satellite imagery.

Additional limitations are specific to the TMM methodology. The unmixing model requires that processing be done on a per-tile basis, adding computational inconvenience when processing over large areas. One important assumption is the linear mixing of a small number of endmembers. While this is generally not limiting for the *spectral mixing* case (Small, 2004; Small and Milesi, 2013; Sousa and Small, 2017), the testing of this assumption has been less thorough for the *temporal mixing* case. Two pieces of supporting evidence for the validity of linear temporal mixing assumption in this study are: 1) the presence of corners and edges in the TFS, suggesting binary linear mixing lines, and 2) the linearity of land cover estimate scaling from 10 to 30 m resolution. However, the observed binary mixing lines are admittedly more ambiguous in the temporal mixing case than the spectral mixing case, and some deviation from the 1:1 line is observed in the spatial scaling investigation. This fundamental question, as well as further considerations about model performance such as the conditioning of the inversion and higher-order complexity due to large non-noise data dimensionality, are interesting and potentially informative. We defer detailed investigation of these factors to a future study.

It is also important to note that the success of the method in the foothill oak study area analyzed here is largely achievable because of the biophysical properties of the landscape. The grassland-savanna-woodland continuum present here is well-suited to a spatial mixing approach that explicitly includes shadow due to the distinctive phenology of Mediterranean-climate winter and spring annuals compared to overstory deciduous or evergreen trees. We have intentionally constrained the geography of the problem to yield a study area which is tractable for our purposes and acknowledge that the method is unlikely to work as well in some other locations as it does here. However, we do note that 1) this study area is spatially extensive and inclusive of much of the range of some of the oak species under consideration, and 2) the properties of this study area likely are generalizable to many other Mediterranean oak systems with comparable levels of floristic and climatic complexity.

5.3. Potential applications and research directions

The simplicity and consistency of the method could be compared to other approaches for monitoring of regional oak cover dynamics and trends due to changing land use (Cameron et al., 2014), climate anomalies such as the 2013–2017 drought (Das et al., 2020; McLaughin et al. 2020), and wildfire (Koltunov et al., 2019; Mallek et al., 2013). Range managers may find the approach useful for monitoring forage amount and rangeland conditions (Li et al., 2012). One strength of the temporal mixture model for such applications is the provision of a continuous field output which can then be geographically delimited and classified to suit specific management and monitoring requirements.

The recent and ongoing surge in remote observational capacity provides a number of avenues of potential research and development. Measurements with higher spatial resolution and/or shorter revisit time (e.g. Planet) might be used to improve measurement density – if critical data quality metrics such as subpixel geolocation and science-grade radiometry are capable of consistently being met. In addition, time series provided by orbital hyperspectral sensors could provide narrowband absorption characteristics at each time step, allowing for more refined biophysical interpretation of the spectral metric used beyond areal photosynthetic vegetation cover (Thenkabail et al., 2018). Landscape partitioning and/or object based analysis using spatially extensive LiDAR could provide further constraints to provide context and improve a multispectral-only approach for prospective monitoring (Bergen et al., 2009; Simonson et al., 2012).

6. Conclusions

The results of this study suggest that single-year temporal mixture models (TMMs) can produce maps of Mediterranean-climate oak woodlands which are spatially consistent, robust to temporal sampling variability, insensitive to differences in Landsat and Sentinel-2 spatial resolution, and compare favorably to airborne and field surveys. The example in Sequoia National Park also suggests that the TMM approach can be further extended to provide useful information about multi-year vegetation dynamics in Mediterranean-climate oak woodlands, especially in the cases of synchronous vegetation community responses following disturbances like drought and fire. Taken together, these results suggest that TMMs may provide a parsimonious, accurate, and scalable framework for assessment and monitoring of Mediterranean-climate oak woodlands.

Declaration of interests

The authors declare that they have no known competing financial interests or personal relationships that could have appeared to influence the work reported in this paper.

Acknowledgements

D. Sousa received financial support from a postdoctoral fellowship from the La Kretz Research Center at Sedgwick Reserve and office and computing support from the National Center for Ecological Analysis and Synthesis (NCEAS). The authors thank managing Associate Editor Geoffrey Henebry and two anonymous reviewers for constructive comments that resulted in improvements to the presentation, clarity, and relevance of this work.

References

Adams, J.B., Gillespie, A.R., 2006. Remote Sensing of Landscapes with Spectral Images: A Physical Modeling Approach. Cambridge University Press.

Adams, J.B., Smith, M.O., Johnson, P.E., 1986. Spectral mixture modeling: a new analysis of rock and soil types at the Viking Lander 1 site. J. Geophys. Res. Solid Earth 91, 8098–8112. https://doi.org/10.1029/JB091iB08p08098.

Allen-Diaz, B., Standiford, R., Jackson, R., 2007. Oak woodlands and forests. In: Barbour, M., Keeler-Wolf, T., Schoenherr, A. (Eds.), Terrestrial Vegetation of California. University of California Press, Berkeley, California, pp. 313–338.

Asner, G.P., Brodrick, P.G., Anderson, C.B., Vaughn, N., Knapp, D.E., Martin, R.E., 2016. Progressive forest canopy water loss during the 2012–2015 California drought. Proc. Natl. Acad. Sci. 113, E249–E255. https://doi.org/10.1073/pnas.1523397113.

Baldwin, B., Keil, D., Markos, S., Mishler, B., Patterson, R., Rosatti, T., Wilken, D., 2020. Jepson Flora Project.

Baldwin, B.G., 2014. Origins of plant diversity in the California Floristic Province. Annu. Rev. Ecol. Evol. Syst. 45, 347–369. https://doi.org/10.1146/annurev-ecolsys-110512-135847.

Berberoglu, S., Akin, A., 2009. Assessing different remote sensing techniques to detect land use/cover changes in the eastern Mediterranean. Int. J. Appl. Earth Obs. Geoinf. 11, 46–53. https://doi.org/10.1016/j.jag.2008.06.002.

Bergen, K.M., Goetz, S.J., Dubayah, R.O., Henebry, G.M., Hunsaker, C.T., Imhoff, M.L., Nelson, R.F., Parker, G.G., Radeloff, V.C., 2009. Remote sensing of vegetation 3-D structure for biodiversity and habitat: review and implications for lidar and radar spaceborne missions. J. Geophys. Res. Biogeosci. 114. https://doi.org/10.1029/2008JG000883.

Berger, M., Moreno, J., Johannessen, J.A., Levelt, P.F., Hanssen, R.F., 2012. ESA's sentinel missions in support of earth system science. Remote Sens. Environ. 120, 84–90.

Bogan, S.A., Antonarakis, A.S., Moorcroft, P.R., 2019. Imaging spectrometry-derived estimates of regional ecosystem composition for the Sierra Nevada. California. Remote Sens. Environ. 228, 14–30. https://doi.org/10.1016/j.rse.2019.03.031.

Borchert, M., Davis, F.W., 2018. Central Coast Bioregion. In: Sugihara, N.G., van Wagtendonk, J.W., Shaffer, K.E., Fites-Kaufman, J., Thode, A.E. (Eds.), Fire in California's Ecosystems. University of California Press, Berkeley, pp. 299–318.

California Department of Fish and Wildlife (CDFW), 2014. California Wildlife Habitat Relationships, Version 9.0 [WWW Document]. https://wildlife.ca.gov/Data/CWHR (accessed 1.9.20).

Cameron, D.R., Marty, J., Holland, R.F., 2014. Whither the rangeland?: protection and conversion in California's rangeland ecosystems. PLoS ONE 9, e103468. https://doi.org/10.1371/journal.pone.0103468.

Chander, G., Markham, B.L., Helder, D.L., 2009. Summary of current radiometric calibration coefficients for Landsat MSS, TM, ETM+, and EO-1 ALI sensors. Remote Sens. Environ. 113, 893–903.

Chi, J., Kim, H.-C., Kang, S.-H., 2016. Machine learning-based temporal mixture analysis of hypertemporal Antarctic Sea ice data. Remote Sens. Lett. 7, 190–199. https://doi.org/10.1080/2150704X.2015.1121300.

Claverie, M., Ju, J., Masek, J.G., Dungan, J.L., Vermote, E.F., Roger, J.-C., Skakun, S.V., Justice, C., 2018. The harmonized Landsat and Sentinel-2 surface reflectance data set. Remote Sens. Environ. 219, 145–161.

Das, A.J., Ampersee, N.J., Pfaff, A.H., Stephenson, N.L., Swiecki, T.J., Bernhardt, E.A., Haggerty, P.K., Nydick, K.R., 2020. Tree mortality in blue oak woodland during extreme drought in Sequoia National park, California. Madroño 66, 164–175. https://doi.org/10.3120/0024-9637-66.4.164.

Davis, F., Baldocchi, D., Tyler, C., 2016. Chapter 25: Oak Woodlands. In: Ecosystems of California. University of California Press, Oakland, CA, pp. 509–529.

Drusch, M., Del Bello, U., Carlier, S., Colin, O., Fernandez, V., Gascon, F., Hoersch, B., Isola, C., Laberinti, P., Martimort, P., 2012. Sentinel-2: ESA's optical high-resolution mission for GMES operational services. Remote Sens. Environ. 120, 25–36.

Elmore, A.J., Mustard, J.F., Manning, S.J., Lobell, D.B., 2000. Quantifying vegetation change in semiarid environments: precision and accuracy of spectral mixture analysis and the normalized difference vegetation index. Remote Sens. Environ. 73, 87–102. https://doi.org/10.1016/S0034-4257(00)00100-0.

Elmore, A.J., Guinn, S.M., Minsley, B.J., Richardson, A.D., 2012. Landscape controls on the timing of spring, autumn, and growing season length in mid-Atlantic forests. Glob. Chang. Biol. 18, 656–674. https://doi.org/10.1111/j.1365-2486.2011.02521.x.

Fisher, J.I., Mustard, J.F., Vadeboncoeur, M.A., 2006. Green leaf phenology at Landsat resolution: scaling from the field to the satellite. Remote Sens. Environ. 15.

Flint, L.E., Flint, A.L., Mendoza, J., Kalansky, J., Ralph, F.M., 2018. Characterizing drought in California: new drought indices and scenario-testing in support of resource management. Ecol. Process. 7, 1. https://doi.org/10.1186/s13717-017-0112-6.

Franklin, J., Davis, F.W., Lefebvre, P., 1991. Thematic mapper analysis of tree cover in semiarid woodlands using a model of canopy shadowing. Remote Sens. Environ. 36, 189–202. https://doi.org/10.1016/0034-4257(91)90056-C.

Fricker, G.A., Ventura, J.D., Wolf, J.A., North, M.P., Davis, F.W., Franklin, J., 2019. A convolutional neural network classifier identifies tree species in mixed-conifer Forest from hyperspectral imagery. Remote Sens. 11, 2326. https://doi.org/10.3390/rs11192326.

Gaman, T., Firman, J., 2006. Oaks 2040: The Status and Future of Oaks in California. California Oak Foundation.

Gillespie, A., 1990. Interpretation of residual images: spectral mixture analysis of AVIRIS images, Owens Valley, California. In: Proc. Second Airborne Visible/Infrared Imaging Spectrometer (AVIRIS) Workshop. NASA, Pasadena, California, pp. 243–270.

Guisti, G., Scott, T., Garrison, B., 1996. Oak woodland wildlife ecology and habitat relationships. In: Guidelines for Managing California's Hardwood Rangelands. Agriculture and Natural Resources. University of California Division of Agriculture and Natural Resources, Berkeley, CA.

Gunning, D., 2017. Explainable artificial intelligence (XAI). Update, Defense Advanced Research Projects Agency (DARPA) Program.

Jain, M., Mondal, P., DeFries, R.S., Small, C., Galford, G.L., 2013. Mapping cropping intensity of smallholder farms: a comparison of methods using multiple sensors. Remote Sens. Environ. 134, 210–223. https://doi.org/10.1016/j.rse.2013.02.029.

Klausmeyer, K.R., Shaw, M.R., 2009. Climate change, habitat loss, protected areas and the climate adaptation potential of species in Mediterranean ecosystems worldwide. PLoS ONE 4, e6392. https://doi.org/10.1371/journal.pone.0006392.

Koltunov, A., Ramirez, C.M., Ustin, S.L., Slaton, M., Haunreiter, E., 2019. eDaRT: the ecosystem disturbance and recovery tracker system for monitoring landscape disturbances and their cumulative effects. Remote Sens. Environ. 111482. https://doi.org/10.1016/j.rse.2019.111482.

Kuemmerle, T., Radeloff, V.C., Perzanowski, K., Hostert, P., 2006. Cross-border comparison of land cover and landscape pattern in Eastern Europe using a hybrid classification technique. Remote Sens. Environ. 16.

Li, S., Potter, C., Hiatt, C., 2012. Monitoring of net primary production in California rangelands using Landsat and MODIS satellite remote sensing. Nat. Res. Forum 3, 720–726. https://doi.org/10.4236/nr.2012.32009.

Li, W., Wu, C., 2014. Phenology-based temporal mixture analysis for estimating large-scale impervious surface distributions. Int. J. Remote Sens. 35, 779–795. https://doi.org/10.1080/01431161.2013.873147.

Liu, Y., Hill, M.J., Zhang, X., Wang, Z., Richardson, A.D., Hufkens, K., Filippa, G., Baldocchi, D.D., Ma, S., Verfaillie, J., Schaaf, C.B., 2017. Using data from Landsat, MODIS, VIIRS and PhenoCams to monitor the phenology of California oak/grass savanna and open grassland across spatial scales. Agric. For. Meteorol. 237–238, 311–325. https://doi.org/10.1016/j.agrformet.2017.02.026.

Loarie, S.R., Carter, B.E., Hayhoe, K., McMahon, S., Moe, R., Knight, C.A., Ackerly, D.D., 2008. Climate change and the future of California's endemic Flora. PLoS ONE 3, e2502. https://doi.org/10.1371/journal.pone.0002502.

Lobell, D.B., Asner, G.P., 2004. Cropland distributions from temporal unmixing of MODIS data. Remote Sens. Environ. 93, 412–422.

Mallek, C., Safford, H., Viers, J., Miller, J., 2013. Modern departures in fire severity and area vary by forest type. Sierra Nevada and southern cascades, California, USA. https://doi.org/10.1890/ES13-00217.1. Ecosphere 4, art153.

Marañón, T., Marañón, T., Pugnaire, F.I., Callaway, R.M., 2009. Mediterranean-Climate Oak Savannas: The Interplay between Abiotic Environment and Species Interactions.

McClaran, M.P., Bartolome, J.W., 1989. Effect of Quercus douglasii (fagaceae) on herbaceous understory along a rainfall gradient. Madroño 36, 141–153.

McLaughlin, B.C., Blakey, R., Weitz, A.P., Feng, X., Brown, B.J., Ackerly, D.D., Dawson, T.E., Thompson, S.E., 2020. Weather underground: subsurface hydrologic processes mediate tree vulnerability to extreme climatic drought. Glob. Chang. Biol. 26, 3091–3107. https://doi.org/10.1111/gcb.15026.

Melaas, E.K., Sulla-Menashe, D., Gray, J.M., Black, T.A., Morin, T.H., Richardson, A.D., Friedl, M.A., 2016. Multisite analysis of land surface phenology in North American temperate and boreal deciduous forests from Landsat. Remote Sens. Environ. 186, 452–464. https://doi.org/10.1016/j.rse.2016.09.014.

Mensing, S., 2006. The History of Oak Woodlands in California, Part II: The Native American and Historic Period.

Miller, J.D., Safford, H.D., Crimmins, M., Thode, A.E., 2009. Quantitative evidence for increasing forest fire severity in the Sierra Nevada and southern Cascade Mountains, California and Nevada, USA. Ecosystems 12, 16–32.

Miraglio, T., Adeline, K., Huesca, M., Ustin, S., Briottet, X., 2020. Monitoring LAI, chlorophylls, and carotenoids content of a woodland savanna using hyperspectral imagery and 3D radiative transfer Modeling. Remote Sens. 12, 28. https://doi.org/10.3390/rs12010028.

Myers, N., Mittermeier, R.A., Mittermeier, C.G., Fonseca, G.A.B. da, Kent, J., 2000. Biodiversity hotspots for conservation priorities. Nature 403, 853–858. https://doi.org/10.1038/35002501.

Navarro, A., Catalao, J., Calvao, J., 2019. Assessing the use of Sentinel-2 time series data for monitoring Cork oak decline in Portugal. Remote Sens. 11, 2515. https://doi.org/10.3390/rs11212515.

Pavlik, B., Muick, P., Johnson, S., 1993. Oaks of California. Cachuma Press, Los Olivos, CA.

Piwowar, J.M., Peddle, D.R., LeDrew, E.F., 1998. Temporal mixture analysis of arctic sea ice imagery: a new approach for monitoring environmental change. Remote Sens. Environ. 63, 195–207.

Quarmby, N.A., 1992. Towards continental scale crop area estimation. Int. J. Remote Sens. 13, 981–989. https://doi.org/10.1080/01431169208904172.

Quarmby, N.A., Townshend, J.R.G., Settle, J.J., White, K.H., Milnes, M., Hindle, T.L., Silleos, N., 1992. Linear mixture modelling applied to AVHRR data for crop area estimation. Int. J. Remote Sens. 13, 415–425. https://doi.org/10.1080/01431169208904046.

Recanatesi, F., Giuliani, C., Ripa, M.N., 2018. Monitoring Mediterranean oak decline in a Peri-urban protected area using the NDVI and Sentinel-2 images: the case study of Castelporziano state natural reserve. Sustainability 10, 3308. https://doi.org/10.3390/su10093308.

Richardson, A.D., Hufkens, K., Milliman, T., Frolking, S., 2018. Intercomparison of phenological transition dates derived from the PhenoCam dataset V1.0 and MODIS satellite remote sensing. Sci. Rep. 8, 1–12. https://doi.org/10.1038/s41598-018-23804-6.

Settle, J.J., Drake, N.A., 1993. Linear mixing and the estimation of ground cover proportions. Int. J. Remote Sens. 14, 1159–1177. https://doi.org/10.1080/01431169308904402.

Simonson, W.D., Allen, H.D., Coomes, D.A., 2012. Use of an airborne Lidar system to model plant species composition and diversity of Mediterranean oak forests. Conserv. Biol. 26, 840–850. https://doi.org/10.1111/j.1523-1739.2012.01869.x.

Small, C., 2001. Estimation of urban vegetation abundance by spectral mixture analysis. Int. J. Remote Sens. 22, 1305–1334. https://doi.org/10.1080/01431160151144369.

Small, C., 2003. High spatial resolution spectral mixture analysis of urban reflectance. Remote Sens. Environ. 88, 170–186. https://doi.org/10.1016/j.rse.2003.04.008. IKONOS Fine Spatial Resolution Land Observation.

Small, C., 2004. The Landsat ETM+ spectral mixing space. Remote Sens. Environ. 93, 1–17. https://doi.org/10.1016/j.rse.2004.06.007.

Small, C., 2012. Spatiotemporal dimensionality and time-space characterization of multitemporal imagery. Remote Sens. Environ. 124, 793–809.

Small, C., 2018. Multisource Imaging of Urban Growth and Infrastructure Using Landsat, Sentinel and SRTM, in: NASA Landsat-Sentinel Science Team Meeting. Rockville, MD.

Small, C., Milesi, C., 2013. Multi-scale standardized spectral mixture models. Remote Sens. Environ. 136, 442–454. https://doi.org/10.1016/j.rse.2013.05.024.

Small, C., Sousa, D., 2019. Spatiotemporal characterization of mangrove phenology and disturbance response: the Bangladesh Sundarban. Remote Sens. 11, 2063. https://doi.org/10.3390/rs11172063.

Smith, M.O., Ustin, S.L., Adams, J.B., Gillespie, A.R., 1990. Vegetation in deserts: I. A regional measure of abundance from multispectral images. Remote Sens. Environ. 31, 1–26. https://doi.org/10.1016/0034-4257(90)90074-V.

Sousa, D., Small, C., 2017. Global cross-calibration of Landsat spectral mixture models. Remote Sens. Environ. 192, 139–149. https://doi.org/10.1016/j.rse.2017.01.033.

Sousa, D., Small, C., 2018. Multisensor analysis of spectral dimensionality and soil diversity in the great Central Valley of California. Sensors 18, 583. https://doi.org/10.3390/s18020583.

Sousa, D., Small, C., 2019. Mapping and monitoring Rice agriculture with multisensor temporal mixture models. Remote Sens. 11, 181. https://doi.org/10.3390/rs11020181.

Sousa, D., Small, C., Spalton, A., Kwarteng, A., 2019. Coupled spatiotemporal characterization of monsoon cloud cover and vegetation phenology. Remote Sens. 11, 1203. https://doi.org/10.3390/rs11101203.

Storey, J., Choate, M., Lee, K., 2014. Landsat 8 operational land imager on-orbit geometric calibration and performance. Remote Sens. 6, 11127–11152.

Strahler, A.H., Woodcock, C.E., Smith, J.A., 1986. On the nature of models in remote sensing. Remote Sens. Environ. 20, 121–139.

Swatantran, A., Dubayah, R., Roberts, D., Hofton, M., Blair, J.B., 2011. Mapping biomass and stress in the Sierra Nevada using lidar and hyperspectral data fusion. Remote Sens. Environ. 2917–2930. https://doi.org/10.1016/j.rse.2010.08.027. DESDynI VEG-3D special issue 115.

Swiecki, T.J., Bernhardt, E.A., Arnold, R.A., 1997. The California Oak Disease and Arthropod (CODA) Database. In: Pillsbury Norman H Verner Jared Tietje William Tech. Coord. 1997 Proc. Symp. Oak Woodl. Ecol. Manag. Urban Interface Issues 19–22 March 1996 San Luis Obispo CA Gen Tech Rep PSW-GTR-160 Albany CA Pac. Southwest Res. Stn. For. Serv. US Dep. Agric, 543-552 160.

Thenkabail, P.S., Lyon, J.G., Huete, A., Lyon, J.G., Huete, A., 2018. Hyperspectral Indices and Image Classifications for Agriculture and Vegetation. CRC Presshttps://doi.org/10.1201/9781315159331.

Tyler, C.M., Kuhn, B., Davis, F.W., 2006. Demography and recruitment limitations of three oak species in California. Q. Rev. Biol. 81, 127–152. https://doi.org/10.1086/506025.

Verbesselt, J., Hyndman, R., Newnham, G., Culvenor, D., 2010. Detecting trend and seasonal changes in satellite image time series. Remote Sens. Environ. 114, 106–115. https://doi.org/10.1016/j.rse.2009.08.014.

Vermote, E., Saleous, N., 2007. LEDAPS surface reflectance product description. Coll. Park Univ, Md.

Vermote, E., Roger, J.-C., Franch, B., Skakun, S., 2018. LaSRC (Land Surface Reflectance Code): Overview, application and validation using MODIS, VIIRS, LANDSAT and Sentinel 2 data's. In: IGARSS 2018–2018 IEEE International Geoscience and Remote Sensing Symposium. IEEE, pp. 8173–8176.

Woodcock, C.E., Loveland, T.R., Herold, M., Bauer, M.E., 2019. Transitioning from change detection to monitoring with remote sensing: a paradigm shift. Remote Sens. Environ. 111558. https://doi.org/10.1016/j.rse.2019.111558.

Wulder, M.A., Masek, J.G., Cohen, W.B., Loveland, T.R., Woodcock, C.E., 2012. Opening the archive: how free data has enabled the science and monitoring promise of Landsat. Remote Sens. Environ. Landsat Legacy Special Issue 122, 2–10. https://doi.org/10.1016/j.rse.2012.01.010.

Yang, F., Matsushita, B., Fukushima, T., Yang, W., 2012. Temporal mixture analysis for estimating impervious surface area from multi-temporal MODIS NDVI data in Japan. ISPRS J. Photogramm. Remote Sens. 72, 90–98. https://doi.org/10.1016/j.isprsjprs.2012.05.016.

Zhang, X., Jayavelu, S., Liu, L., Friedl, M.A., Henebry, G.M., Liu, Y., Schaaf, C.B., Richardson, A.D., Gray, J., 2018. Evaluation of land surface phenology from VIIRS data using time series of PhenoCam imagery. Agric. For. Meteorol. 256–257, 137–149. https://doi.org/10.1016/j.agrformet.2018.03.003.